Creation and Reconstruction of Thermochromic Au Nanorods with Surface Concavity

Zhiwei Li^a, Jian Zhang^a, Jianbo Jin^a, Fan Yang^a, Rashed Aleisa^a, and Yadong Yin^{a*}

^aDepartment of Chemistry, University of California, Riverside, CA 92521 (USA)

KEYWORDS: templated synthesis, Au nanorods, localized surface plasmon resonance, surface concavity, structural reconstruction, thermochromic response, color

ABSTRACT: Conventional colloidal syntheses typically produce nanostructures with positive curvatures due to thermodynamic preference. Here we demonstrate the creation of surface concavity in Au nanorods through seed-mediated growth in confined spaces and report their thermochromic responses to temperature changes. The unique surface concavity is created by templating against Fe₃O₄ nanorods, producing a new concavity-sensitive plasmonic band. Due to the high surface energy, the metastable nanorods can be reconstructed at a moderate temperature, enabling convenient and precise tuning of their plasmonic properties by aging in different solvents. Such structural reconstruction of concave Au nanorods enables the fabrication of thermochromic plasmonic films that can display images with vivid color changes or exhibit encrypted, invisible information upon aging. This templating strategy is universal in creating concave nanostructures, which may open the door to designing new nanostructures with promising applications in sensing, anti-counterfeiting, information encryption, and displays.

1. Introduction

Colloidal nanostructures of noble metals have attracted increasing attention due to their unique optical, electronic, and catalytic properties.¹⁻⁵ Their localized surface plasmon resonance (LSPR) features sharp absorption peaks, localized electric field enhancement, and tunable colors complementary to the peak position, which have great potentials in developing high-performance sensors, 6-8 catalysts, 9 and smart optical devices. 10-12 Among these established applications, dynamic switching of plasmonic colors has attracted great attention due to many compelling advantages of plasmonic nanostructures in the color generation, such as high tunability, sharp LSPR peaks, and widely accessible colors in the whole visible spectrum, which have inspired extensive studies on colorimetric responses of plasmonic nanostructures to various stimuli, including chemicals, pH, heat, magnetic and electric fields. 13-15 However, most current studies have focused on color switching of dispersed plasmonic nanoparticles in a solution. Realizing dynamic and controllable color switching in solid films remains challenging, although it is highly desirable in developing practical optical devices. A major obstacle limiting further development is the lack of synthetic approaches to metal nanostructures with sufficient responses to surrounding physicochemical changes. Previous studies have reached an agreement that metal nanocrystals with unconventional surface concavity have superior sensing and catalytic performances over nanostructures with positive curvatures because of the exposure of high-index facets and improved electric field enhancement. 16-20 From the thermodynamic point of view, such concave nanostructures are not stable, offering new opportunities to design novel materials with colorimetric responses.21-23

The conventional solution-based methods of creating surface concavity in plasmonic nanostructures rely on promoting the growth of high-energy facets using secondary

metal atoms or capping ligands.²⁴ The introduction of secondary metal atoms, mostly plasmonically inactive, often significantly deteriorate the plasmonic properties of the resulting nanostructures, albeit their exciting potential for catalytic applications.²⁵⁻²⁶ The selective adhesion of capping ligands has also been employed to produce concave plasmonic nanostructures, such as those with cuboidal and trisoctahedral shapes.²⁷⁻²⁸ Since selective binding is very specific to the ligand/metal facet combination, such a strategy is not general for creating concave nanostructures. Also, the high surface energy of the resulting surface concavity makes it extremely challenging to extend the processes for producing nanostructures of reduced sizes. More importantly, the as-created surface concavity is often small due to the limited contrast of binding energy of ligands on different facets, providing few opportunities for active tuning of the plasmonic properties. A promising method recently emerged by combining selective deposition and etching to synthesize complex metal nanostructures with tunable concavity.²⁹⁻³⁰ However, its evolution into a general platform for the synthesis of concave plasmonic nanostructures requires additional efforts as it involves complex chemical reactions, plasmonically inactive metals, and dynamic organic-inorganic interfaces. 31

In this work, we report a general and efficient method to create pronounced, highly tunable surface concavity in Au nanorods, which can be further meticulously tailored by inducing structure reconstruction in confined spaces. By confining the seed-mediated growth of Au in a well-defined space containing an iron oxide nanorod, we demonstrate the production of concave Au nanorods whose surface concavity is determined by the nanorod template. Further, we take advantage of the magnetic property of the iron oxide nanorods and the thermodynamic instability of the Au nanorods to design solid thermochromic plasmonic films that

^{*}Email: yadong.yin@ucr.edu

can display rich color changes or exhibit encrypted, invisible information in response to temperature changes. Our results demonstrate that nanostructure engineering combined with confined-space chemical transformation may offer exciting opportunities to design unconventional nanostructures for smart optical materials and devices.

2. Experimental section

2.1. Synthesis of FeOOH nanorods. The uniform FeOOH nanorods were synthesized by hydrolysis of FeCl3 in aqueous solutions. For synthesizing FeOOH nanorods with 110 nm in length and 20 nm in width, 10.812 g of FeCl₃ (40 mmol) was dissolved in 400 mL of Milli-Q water. The solution was placed in an oven at 87 °C for 18 hours. The precipitated FeOOH nanorods were washed three times with deionized (DI) water and dispersed in 40 mL of water. For preparing thicker FeOOH nanorods, 0.1 M of FeCl3 was added to 400 mL of HCl solution. The concentrations of HCl were 0.06 M and 0.04 M for FeOOH nanorods with diameters of 25 nm and 35 nm, respectively. The prepared solution was kept at 87 °C for 25.5 hours. The FeOOH nanorods were washed by water three times and then dispersed in 40-mL water. FeOOH nanorods with a diameter of 70 nm were prepared by hydrolysis of FeCl₃ (0.1 M) at room temperature. In our experiments, 4 L of FeCl₃ (0.1 M) was prepared and sealed in a plastic bottle, which was kept at room temperature for 6 months. Afterward, the precipitated nanorods were washed three times by DI water and dispersed in 400 mL of water for further use. The synthesis of FeOOH is scalable and suitable for large-scale production.

2.2. SiO2 coating on FeOOH nanorods. FeOOH nanorods were first modified with polyacrylic acid (PAA). Typically, 5 mL of the FeOOH (100 nm × 20 nm) solutions were added into 300 mL of DI water containing 108 mg of PAA. The solution was magnetically stirred overnight, and excess PAA was removed by washing with DI water three times. The precipitated FeOOH-PAA nanorods were re-dispersed in 15 mL of DI water. 3 mL of the FeOOH-PAA was used for silica coating. In a typical process, 1mL of NH₃ and 20 mL of ethanol were added in sequence. The mixture was sonicated for ~10 minutes to fully disperse FeOOH-PAA nanorods. Then, 100 μL and 200 μL of tetraethoxysilane (TEOS) were used for silica of 3 nm and 8 nm, respectively. For achieving 12 nm silica, another 200 µL of TEOS was added 1 hour after the first 200-µL TEOS. The reaction continued for 1 hour. After silica coating, the FeOOH@SiO₂ was precipitated out by centrifugate (15000 rpm for 10 minutes) and washed with water three times. For thicker FeOOH nanorods, 3 mL of the stock solution was added to 120 mL of DI water containing 43.2 mg of PAA. The mixture solution was stirred overnight. The FeOOH-PAA nanorods were recovered by washing with water three times and then dispersed in 12 mL of DI water. A 3-mL solution of FeOOH-PAA nanorods was used for silica coating. 1 mL of NH₃ and 20 mL of ethanol were added to the solution, which was sonicated for ~ 10 minutes to fully disperse nanorods. For the silica layer of 35 nm, 100 µL of TEOS was added twice with a 30-minute interval. The silica-coated FeOOH nanorods were washed by DI water three times (11000 rpm for 6 minutes). For producing a thin silica layer on FeOOH nanorods with a diameter of 70 nm, 30 μL of TEOS was added, and the reaction lasted for 30 minutes.

2.3. Synthesis of magnetic nanorods. The high-temperature polyol reduction was used to convert FeOOH into Fe₃O₄. In a typical process, 30 mL of diethylene glycol (DEG) was heated to 220 °C in a three-neck round bottle flask. The above FeOOH@SiO₂ solution was concentrated to less than 50 μ L of DI water. The solution was then injected into the hot DEG slowly. The reaction was stirred at 220 °C for 5 hours. After reduction, Fe₃O₄@SiO₂ nanorods were washed with DI water three times.

2.4. Au seeds preparation and attachment. 12 uL of THPC and 250 mL of NaOH (2M) were added to 45-mL water. After stirring for 5 minutes, 2 mL of HAuCl₄ (1%) was added to the above solution. The Au seed (Aus) solution was aged at dark overnight. The $Fe_3O_4@SiO_2$ nanorods were modified by 3-aminopropyltriethoxysilane (APTES) in ethanol. In a typical process, magnetic nanorods were dispersed in ethanol and heat at 87 °C under refluxing. 2 mL of APTES was added, and the solution was kept at this temperature for 5 hours. After modification, the rods were washed three times by ethanol to remove excess APTES and then DI water three times. Au seeds were attached to APTES-modified magnetic nanorods by stirring their mixture (25 mL) for 1 hour and removing excess Au seeds by magnetic separation.

2.5. Resorcinol-formaldehyde (RF) coating. RF coating was facilitated by modifying Fe₃O₄@SiO₂/Aus nanorods by polyvinylpyrrolidone (PVP). The rods were first dispersed in 35 mL of water, and 5 mL of PVP (10 mg/mL) was added. The mixture was stirred overnight. Nanorods were recovered by centrifugation, washed three times by DI water, and dispersed in 10 mL of water. 5 mL of rod dispersion was added into 25 mL of water. Afterward, 15-mg resorcinol (R) and 21-µL formaldehyde (F) were added. The temperature was increased to 50 $^{\circ}$ C, followed by the addition of 100 μ L of 2.8% NH₃. After heating at 50 °C for 1.5 hours, the temperature was raised to 100 °C and maintained for another 3 hours for condensation. Then, it was cooled down to room temperature and washed with DI water three times. The final product was dispersed in 2 mL of Milli-Q water for further seeded growth.

2.6. Seeded growth. In a typical process, 500 µL of PVP (20mg/mL, MW=10000), 100 μL of KI (0.2 M), 100 μL of AA (0.1M), 15 µL of HAuCl₄ (0.25M) were sequentially added into 2 mL of Milli-Q water. The solution turned brown right after dropwise adding HAuCl4 and then colorless within a few seconds. After that, 25 µL of seed solution was quickly injected into the solution. The growth normally took ~10 minutes. For growing Ag, 200 µL of PVP (Mw=10000, 20 mg/mL), 50 µL of seed solution, and 200 µL of formaldehyde (reducing agent) were added into 2-mL Milli-Q water in sequence and reacted at 80 °C for 10 minutes. For growing Cu, 200-μL PAA (18mg/mL), 120-μL hydrazine hydrate as reducing agent, 20μL CuCl₂ (0.2M), 50-μL seed solution were added in sequence into 2-mL Milli-Q water and reacted at 60 °C for 30 minutes. After reduction, the hybrid nanorods were washed by water three times and dispersed in water for further characterization.

2.7. Aging of concave Au nanorods. The structural reconstruction was carried out by heating a dispersion of concave Au nanorods in DI water, ethanol, or DMF in an oil bath at 60 °C for different periods. Extinction spectra of the solution were measured at certain time intervals.

2.8. Characterization. Ultraviolet-visible-near infrared (UV-Vis-NIR) spectra were measured by Ocean Optics HR2000 spectrometer. TEM images were taken on Tecnai 12 transmission electron microscope operating at 120 kV. For measuring the spectra under polarized light, a commercial polarizer was introduced right before the sample. Meanwhile, a uniform magnetic field was applied at \sim 0.5 cm.

3. Results and Discussion

3.1. Creation of concavity on Au nanorods. The unconventional synthesis involves the seeded growth of Au in defined gaps between Fe₃O₄ nanorods and their enclosing polymer shells (**Figure 1a**). $^{32-33}$ A typical process began with the preparation of Fe₃O₄@SiO₂ nanorods of different sizes by synthesizing FeOOH nanorods using a hydrothermal reaction (**Table s1**), coating them with a silica layer, and then reduction by diethylene glycol at 220 °C. The surface of Fe₃O₄@SiO₂ nanorods was modified with APTES, attached by Au seeds via electrostatic interactions, ^{12, 34} and further coated with RF resin. $^{35-36}$ The SiO₂ layer was etched away under the basic condition during RF coating, forming a well-defined gap between the Fe₃O₄ nanorod and RF shell (**Figure 1b**).

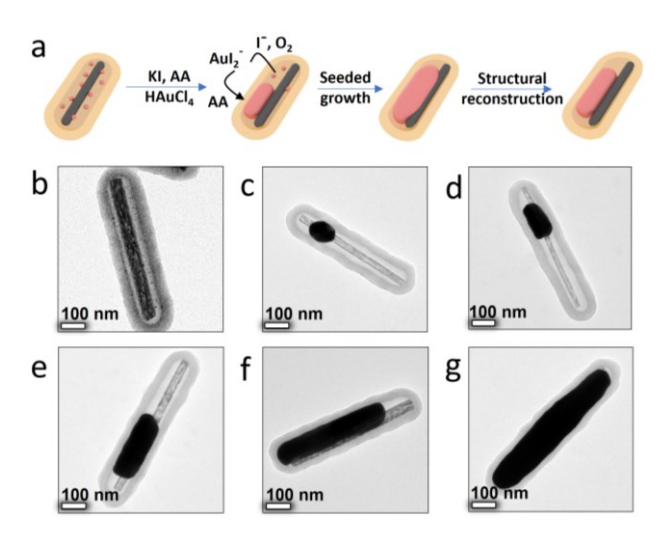


Figure 1. The creation of thermochromic Au nanorods with concavity using space-confined seed-mediated growth. **(a)** Schematic illustration of the space-confined growth and reconstruction of the concave Au nanorods. Au and Fe_3O_4 are represented by red and black colors, respectively, and the RF coating is illustrated by the orange shells. Growth intermediates of the concave Au nanorods with large Fe_3O_4 nanorods as templates (600 nm × 35 nm). **(b-g)** TEM images after seeded growth for 0, 1, 3, 5, 7, 10 minutes, respectively.

The seeded growth of Au was ensured using I^{-} as a strong coordination ligand to Au^{3+} to reduce the reduction potential and minimize self-nucleation. A growth solution was

prepared by sequentially adding PVP, KI, ascorbic acid (AA), and HAuCl4 to Milli-Q water.37 The chloride in AuCl4- was first replaced by iodide, yielding intermediate AuI4- as evidenced by the change of the solution color to brown.³⁸⁻³⁹ Shortly, the solution turned colorless, indicating the further reduction of AuI⁴⁻ to AuI²⁻,⁴⁰ which has a lower reduction potential of +0.58 V than +0.93 V of AuCl4-. The growth of highquality Au nanorods benefited from Ostwald ripening, which was promoted by I- and the dissolved oxygen.⁴⁰ At 1 minute upon mixing the growth and seed solutions, Au seeds inside RF shells ripened into larger ones, which further grew isotropically into Au nanospheres (Figure 1c) until reaching the gap size. Their subsequent growth became one-dimensional owing to the shell confinement (Figures 1d-1g). To understand the Ostwald ripening pathway, we added KI to the Au seed solution at ambient conditions, which interestingly turned into bright red with a pronounced plasmonic peak at ~ 520 nm, indicating the formation of large Au nanoparticles (Figures s1a and s1b). Conversely, if H₂O₂ was added instead of KI, there were no obvious changes in the dark brown solution (Figures s1c and s1d), confirming the critical role of I in the ripening process due to its strong coordination to Au⁺.⁴¹

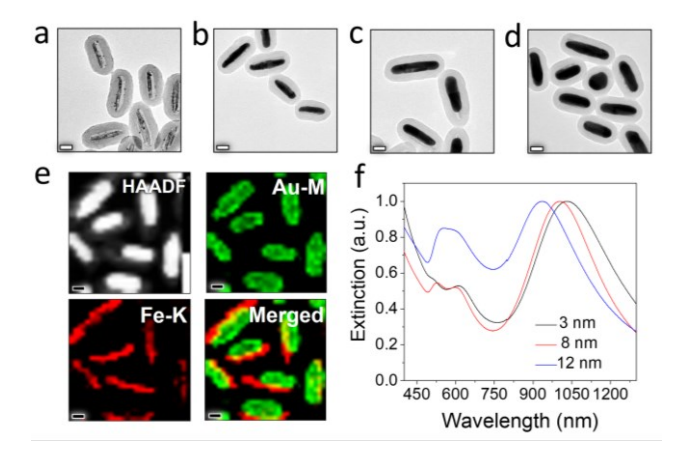


Figure 2. (a) TEM image of Fe₃O₄@gap/Aus@RF. TEM images of the hybrid nanorods after seeded growth within gaps of different thicknesses: **(b)** 3 nm, **(c)** 8 nm, and **(d)** 12 nm. **(e)** High-angle annular dark-field (HAADF) image (left panel) and EDS mapping images of the hybrid structures (right three panels). **(f)** Extinction spectra of hybrid nanorods after seeded growth within nanogaps of different thicknesses. Scale bars: 50 nm.

The thickness of the silica layer was firstly tuned to study how the templates affect the surface concavity of the resulting Au nanorods. Using Fe $_3$ O $_4$ nanorods of 110 nm×20 nm wrapped in 30-nm RF shells as the templates (**Figure 2a**), we varied the thickness of the silica shells from 3 to 8 and 12 nm and produced Au nanorods of increasing thicknesses (**Figures 2b-2d**). The Fe $_3$ O $_4$ nanorods created apparent concavity on the Au rods due to the templating effect, as evidenced by hybrid nanorods with side-by-side configuration. The heterogeneous elemental signals of Au and Fe in **Figure 2e** demonstrate perfect parallel alignment and a precise one-to-one ratio of the Janus nanorods. Rotating the

hybrid nanorod by 15° in TEM revealed a gradual shift in the relative positions of the nanorods from side-by-side to the overlapping configuration (**Figure s2a**), confirming the presence of surface concavity in Au nanorods with different configurations.

3.2. Optical properties of concave Au nanorods. We then measured the extinction spectra of nanorods in realtime to monitor the formation of surface concavity using Fe₃O₄ rods with 8-nm silica coating as templates (**Figure** s2b). The successive one-dimensional growth is evidenced by the gradual redshift of the main plasmon band and a simultaneous color change of the solution from light yellow to dark blue and brown (insets in Figure s2b). An abnormal plasmonic peak was observed at 625 nm at ~5 minutes, with gradually increased intensity and a slight blueshift during the growth, which also existed in the other two samples with 3-nm (Figure s3a) and 12-nm silica nanoshells (Figure s3b). As shown in Figure 2f, the longitudinal plasmon band and the abnormal band (peaks between 590 nm and 625 nm) blueshifted because of decreased aspect ratios when gap size increased from 3 nm to 12 nm. With a larger gap size, the nanorods have a rounder morphology and thus the new band blueshifts. The thickness of the RF shells is crucial in determining product uniformity. For example, a thin RF shell of ~10 nm produces Au nanorods with irregular shapes and nonuniform sizes due to the weak confinement (Figures s4a and s4b), whose size distribution is much broader than the products made of 30-nm RF shells (**Figures s4c** to **s4e**). To understand the optical properties of the concave Au nanorods, we calculated the extinction, scattering, and absorption cross-sections (abbreviated as ECS, SCS, and ACS, respectively) of the Au nanorods synthesized by templating against 8-nm SiO₂ nanoshells (Figure s5). By changing the rod orientation from 0° to 90° with a step of 15°, as illustrated in Figure 3a, we calculated the optical cross-sections using the simulation method depicted in **Figure s5**. The new plasmon band at 625 nm appeared only when Au nanorods were parallel to the light incidence (|90°>), demonstrating a new transverse plasmon band because the resonant oscillation of free electrons only occurs along the rod short-axis under such excitation (**Figure 3b**). This transverse mode is highly dependent on the concavity opening relative to light polarization, with maximum strength at |0°> (Figure 3c) and scattering-dominated plasmonic properties (Figures 3d, s7a, and s7b). The surface energy flux (Poynting vector) and localized electric field distribution in Figure s7c further suggest highly localized and orientation-dependent scattering on the surface concavity.

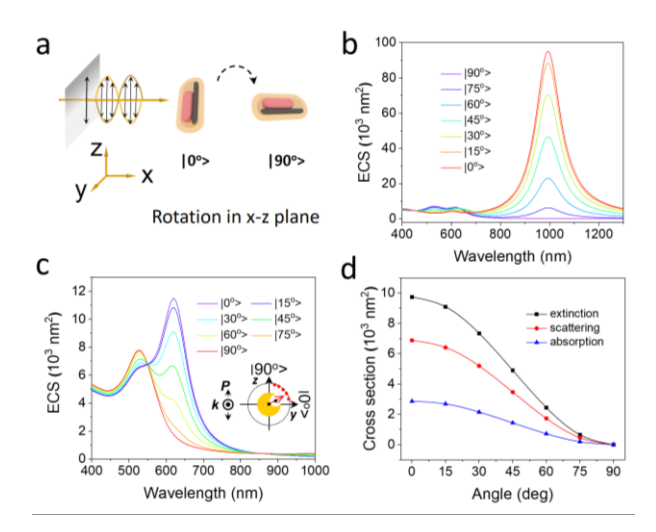


Figure 3. (a) The concave Au nanorod is rotated in the x-z plane while its extinction cross-section is calculated. **(b)** The calculated extinction spectra under various orientations. **(c)** Calculated extinction cross-sections of the transverse mode under different concavity opening directions. The red arrow in the inset indicates the opening direction of the concave Au nanorods. **(d)** Summary of the optical cross-sections of concave Au nanorods at the second transverse band under different opening directions.

We can control the template diameter to precisely tune the surface concavity and the concavity plasmon band of the Au nanorods. As shown in **Figures 4a-4c**, the diameters (r₁) of Fe₃O₄ rods are 25 nm, 35 nm, and 70 nm, respectively, while the thickness of sacrificial silica (r_2) remains ~ 20 nm. Au is directed to grow into a rod with its surface concavity complementary to the curvature of Fe₃O₄ nanorods, leading to a gradual decrease in the surface concavity $(1/r_1)$ and an increase in transverse anisotropy (simply estimated by 1+ $r_1/2r_2$). If 70-nm thin magnetic nanorods with 5-nm SiO₂ layers are used, the seeded growth confined in the narrow space produces boat-like Au nanostructures with the highest transverse anisotropy (theoretical value of 8) among the four samples (Figure 4d). In Figure s8, the increase in transverse anisotropy causes the cavity plasmon modes to redshift from 670 nm to 870 nm. The prepared concave Au nanorods are in a metastable state far away from thermodynamic equilibrium but favored by reduction kinetics.^{28,42-}

This method can be readily extended to other concave nanostructures with different chemical compositions and shapes, for example, producing concave Ag and Cu nanorods by changing the metal precursors during seeded growth. As shown in the TEM images in Figures s9a and **s9b**, Ag and Cu nanorods are formed inside the gaps, and the presence of Fe₃O₄ nanorods creates similar surface concavity on nanorods due to the templating effect. The surface concavity of Ag nanorods is also confirmed by the extinction spectrum in Figure s9c, which exhibits a cavity band at 560 nm in addition to the conventional transverse and longitudinal bands at 415 nm and 960 nm, respectively. The extinction spectra of Cu nanorods in Figure s9d also have three peaks, with the cavity band at 700 nm, first transverse band at 600 nm and longitudinal band at 935 nm. While the sharp longitudinal peaks are consistent with the uniform shape of the products, the presence of the middle cavity bands demonstrates the versatility of this method in producing concave nanorods. The overall shape of the concave nanostructures is determined by that of the initial templates. For example, we prepared Au nanospheres each containing one concavity, using 15-nm Fe $_3$ O $_4$ nanospheres as the initial templates (**Figure s10**). At the early stage during seeded growth, the multiple Au seeds inside RF shells disappear. One large Au nanoparticle grows within each gap due to the ripening of small Au seeds, eventually producing Au nanospheres, each containing one concavity.

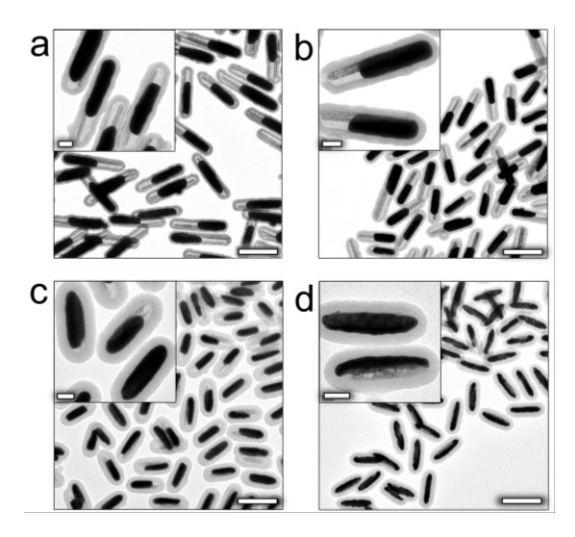


Figure 4. TEM image of hybrid nanorods by using Fe₃O₄ rods with a diameter of **(a)** 25 nm, **(b)** 35 nm, **(c)** 70 nm as templates. The silica thickness is \sim 20 nm in the three samples. **(d)** TEM image of hybrid nanorods prepared using Fe₃O₄ rods of 35-nm diameter and silica shells of \sim 5 nm as templates. Scale bars: 0.5 μ m. Scale bars in insets: 100 nm.

3.3. Structural reconstruction and thermochromic responses. By taking advantage of its metastable nature, we further demonstrate that the surface concavity can be meticulously tailored through structural reconstruction. As shown in **Figures 5a** and **5b**, upon aging of the particles in solution, the surface concavity gradually disappeared, and the Au-Fe₃O₄ boundary became easily distinguishable, along with the gradual blueshift of both longitudinal and cavity bands (Figure s11). As the shell confinement contributes to the formation of high-energy surface curvature, it is possible to precisely tune the reconstruction kinetics by controlling the permeability of the RF shells. Many polar solvents, such as dimethylformamide (DMF), can easily swell RF resin and dissolve short chains due to the high polarity of RF oligomers, making the shell softer and more porous. 44 As a result, the migration of Au atoms from the most energetic domains becomes much easier, which further reduces the nanorod aspect ratio and causes the longitudinal peak to shift from 950 nm to 700 nm (**Figure 5c**). Meanwhile, the cavity plasmon band gradually blueshifted and finally merged with the classic transverse band at 550 nm. It has been generally accepted that the rounding of sharp edges of plasmonic nanoparticles is responsible for the shift of plas-

mon bands but typically with small magnitudes. For example, there would be only a 60-nm shift in the plasmon band of Ag nanoprisms with comparable sharpness and thickness, 45-46 which is much smaller than the 250-nm shift in our concave case. The significant change in the surface curvature and morphology is the primary reason for such a significant shift in plasmon bands. 47-48 In the case of water and ethanol, the shift in the two bands was slower and smaller than that in DMF, with only a 150-nm shift in the longitudinal mode (**Figure 5d**).

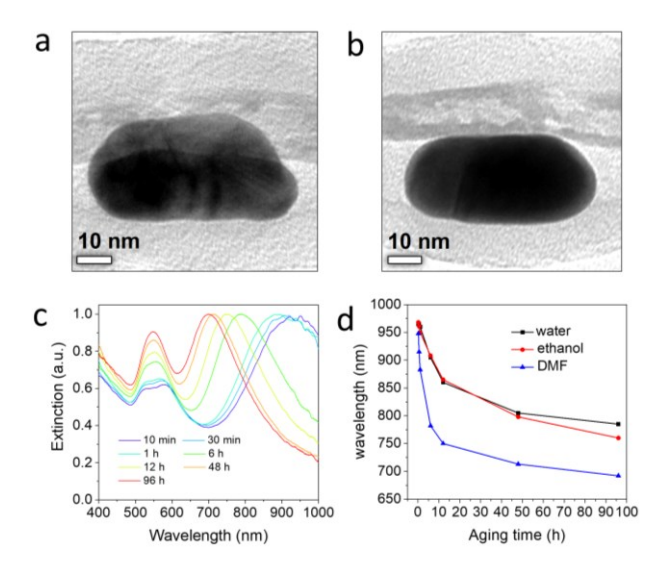


Figure 5. High-magnification TEM images exhibiting the concavity of Au nanorods **(a)** before and **(b)** after aging. **(c)** The extinction spectra of the concave Au nanorods during aging at 60 °C. **(d)** The peaks shift of plasmon band during aging at 60 °C in different solvents.

To further depict the reconstruction of surface concavity upon aging, we carried out a numerical simulation based on the finite element method. The construction and geometry parameters of the 3D model of the hybrid nanostructure are illustrated in **Figure s12a** and **Table s2**. The 3D model was deliberately designed with a constant volume considering the negligible mass loss during structural reconstruction while rod surface area decreased significantly due to the disappearance of surface concavity (Figure s12b). In Figures 6a, s13, and s14, we observed a continuous blueshift in the extinction, scattering, and absorption of both the longitudinal and cavity plasmon bands. In addition to creating surface concavity on Au, another benefit associated with the magnetic nanorods is their preferential parallel alignment along a magnetic field: the orientation and plasmonic excitation of the coupled Au nanorods can be precisely controlled using a magnetic field.^{8, 49-50} This unique property is not affected by the aging process, making the reconstructed nanorods still responsive to a magnet. We measured the extinction spectra of the aged Au nanorods by applying a magnetic field and carefully controlling the field direction (Figure s15a), demonstrating gradually enhanced transverse mode and simultaneously suppressed longitudinal mode from $|0^{\circ}\rangle$ to $|90^{\circ}\rangle$ as shown in **Figure s15b**. This property enables us to distinguish the peak shift of individual mode

during aging by applying a magnet (**Figure s16**). Under linearly polarized light, the cavity band at 600 nm blueshifted until it overlapped with the classic transverse band (left panel in Figure 6b), while the longitudinal plasmon band exhibited a blueshift from 725 nm to 675 nm (right panel in Figure 6b) when Au nanorods were aged for two days at 60 °C. The experimentally observed shifts of plasmon bands are consistent with our simulation results (Figure 6c). The Poynting vectors and the localized electric fields in Figure 6d confirm the decreased scattering strength during the aging process. Notably, the gradual blueshift of the longitudinal LSPR peak is mainly induced by the decrease of rod aspect ratios, while the disappearance of the transverse peak is attributed to the reconstruction of the surface cavity. Both transformations are promoted by the concave feature of the metastable Au nanorods.

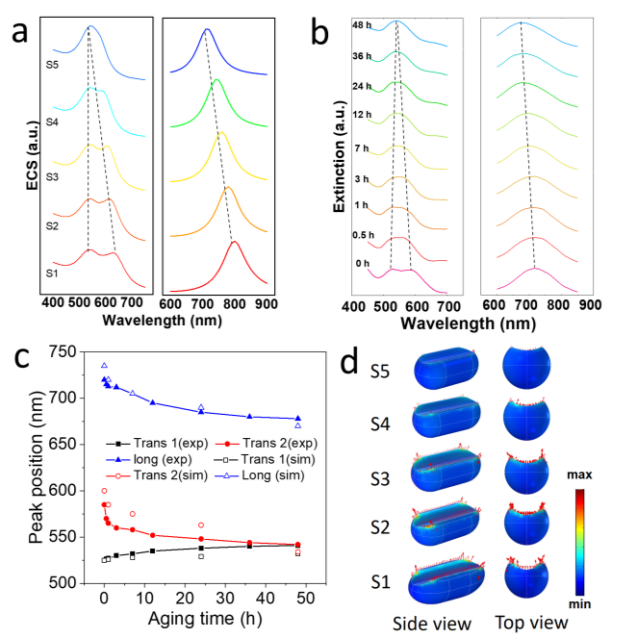


Figure 6. (a) Simulated ECS of the concave Au nanorods during surface reconstruction. The Left and right panels represent the transverse and longitudinal modes, respectively. **(b)** Experimental extinction spectra of the concave Au nanorods during aging at 60 °C for different times. Left and right panels represent the transverse and longitudinal modes, respectively, which is achieved by applying a magnetic field during the measurement. (c) Summary of peak shift of the plasmon bands over aging time. Exp and sim represent experimental and simulated results, respectively. Trans 1, Trans 2, and long indicate classic transverse mode, concavity transverse mode, and longitudinal mode, respectively. (d) The scattering (red arrows) of the concave Au nanorods over aging. The localized electric fields are represented by surface color. The concavity opening directions are 0° under the excitation of 600-nm light.

The surface concavity can be created and removed by controlling the regrowth and aging of Au nanorods in the confined spaces. As shown in **Figures 7a-7c**, the length and surface concavity of the nanorods decreased during the first

aging process and then increased during the following additional seeded growth. The corresponding extinction spectra show a gradual blueshift of the longitudinal plasmon band and the disappearance of the concave band as the nanorod aspect ratio decreased from 2.25 to 1.6 during aging (Fig**ure 7d**), and then a redshift of the longitudinal band during the regrowth of the aged nanorods due to the increasing aspect ratio (Figure 7e). It should be noted that seeded growth of Au nanorods may occur along both lateral and axial directions since RF shells become more deformable after aging in solvents, leading to less defined location of the concavity in the regrown nanorods. The cavity band recovered at 600 nm, consistent with its initial position in Figure 7d. These spectral results demonstrate the reversible tuning of the surface concavity over a broad range. When the Au nanorods were subject to aging again, a similar blueshift of the two bands was observed (Figure 7f). Fig. 7g shows the consistent changes in aspect ratio and the longitudinal resonance band during the growth-aging cycles.

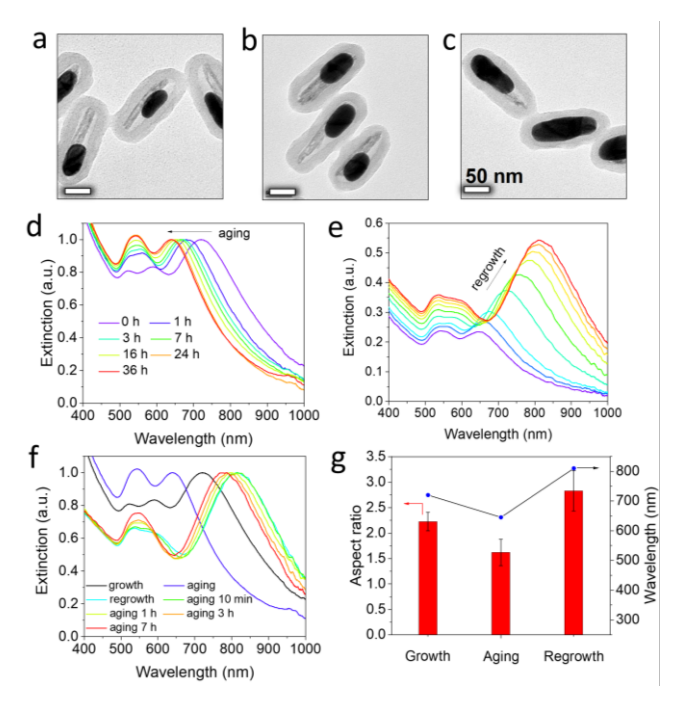


Figure 7. TEM image of hybrid nanorods **(a)** before and **(b)** after aging and **(c)** after the second seeded growth process. **(d)** The corresponding extinction spectra of hybrid nanorods during the first aging. **(e)** The extinction spectra, measured every 30 seconds, of hybrid nanorods after the second seeded growth process. **(f)** The extinction spectra of hybrid nanorods after second aging. **(g)** Summary of the aspect ratios and peak positions of longitudinal modes during the sequential seeded growth and aging process.

3.4. Thermochromic plasmonic films. By taking advantage of the metastable nature of the Au nanorods and the magnetic property of the Fe₃O₄ nanorods, we use the hybrid nanorods to further develop a thermochromic plasmonic film that could display designated images with dynamic color changes or exhibit encrypted information upon aging.

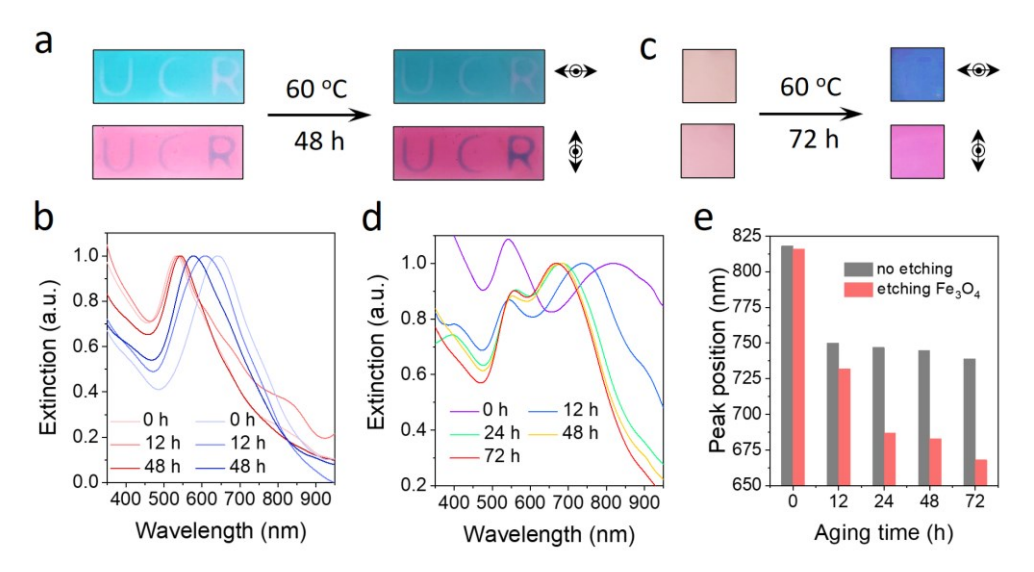


Figure 8. The use of concave Au nanorods for thermochromic plasmonic films. **(a)** Digital images of a plasmonic film made of short Au nanorods and its thermochromic responses to aging. For displaying images under polarized light, the hybrid nanorods were aligned horizontally and vertically in the background and letter regions, respectively. **(b)** The corresponding peak shift during the aging process. The transverse and longitudinal modes are presented in red and blue, respectively. **(c)** Digital pictures of plasmonic films made of Fe_3O_4/Au nanorods after selectively etching Fe_3O_4 nanorods. **(d)** The peak shift during the aging of the concave Au nanorods after etching Fe_3O_4 nanorods. The initial longitudinal peak position is located at 816 nm. The black dots and arrows indicate the light propagation direction and polarization, respectively. **(e)** Time-dependent longitudinal peak positions during the aging of the films before and after selectively etching Fe_3O_4 nanorods.

This strategy is enabled by magnetically aligning the hybrid nanorods in photocurable polymer substrates, during which a photomask is introduced to form patterns with different rod alignment in each color domain. Specifically, the alignment of Au nanorods in the letters and background is vertical and horizontal in **Figure s17a**, respectively. Under a horizontally polarized light, the letters and background appear red and blue due to the selective excitation of the transverse and longitudinal mode of the embedded nanorods, respectively (top panel in **Figure s17b**). Changing the light polarization to a vertical direction alters the excited plasmon modes and switches the colors in these two regions (bottom panel in Figure s17b). To promote the reconstruction of Au nanorods, we created additional space by selective etching of Fe₃O₄ nanorods in the solid film using oxalic acid (Figure s18), which enhances the thermochromic responses. We started with short Au nanorods with a longitudinal LSPR peak at 640 nm, and the complementary color to these peak changes from cvan to blue upon aging at 60 °C for 72 h (Figure 8a). The spectral measurement indicates a blueshift of the peak to 581 nm, consistent with the perceived color changes (Figure 8b). However, when the Fe304 nanorods are not etched away, the film displays negligible color changes, and the final peak is at 605 nm after thermal treatment for 72 h (Figures s19a and s19b). If concave Au nanorods with large aspect ratios are used, the thermochromic plasmonic film can exhibit rich color changes. **Figure 8c** shows the color changes of a plasmonic film made of concave Au nanorods with a longitudinal peak at 816 nm. Because this LSPR peak is in the near-infrared region, there is no noticeable color contrast under different polarization for the plasmonic film both before (left panels in Figure s19c) and after etching Fe₃O₄ nanorods (left panels in Figure 8c). After acid etching and thermal aging, the

plasmonic film exhibits red and blue colors if only the longitudinal and transverse mode is selectively excited, respectively (right panels in Figure 8c). A close spectral measurement ascribes this remarkable thermochromic response to the enhanced shift from 816 nm to 668 nm of the longitudinal peak in the etched film (Figure 8d), which is much larger than the shift in non-etched film (from 818 nm to 739 nm in Figures s19c and s19d). The time-dependent longitudinal peak positions during the aging of the films before and after selectively etching Fe₃O₄ nanorods are summarized in Fig. 8e. The result presented in the two systematic studies demonstrates that selective etching of Fe₃O₄ nanorods can significantly promote the structural reconstruction of concave Au nanorods and enhance the aging kinetics and thermochromic response of the solid film. Two images in the left two panels in Figure 9a imply that the acidic etching does not significantly affect the film's color at ambient conditions. Only upon aging will the film color change from green to blue if a short Au nanorod is used (right panels in Figure 9a).

Another conclusion from the simple comparison between these two experiments is that the thermochromic responses of plasmonic films are highly related to the initial longitudinal peak position of the employed Au nanorods. This observation is beneficial to create thermochromic plasmonic films with customizable color changes. To further explain this effect, we prepared three plasmonic films made of concave Au nanorods with longitudinal peaks at 720 nm, 760 nm, and 860 nm (**Figure s20**). For the 720-nm sample, the peak shifts to 625 nm, leading to color changes from light green to green and cyan. For the 760-nm sample, its peak shifts to 635 nm, and its initial peak position at the visible-

NIR boundary causes negligible contrast (left panels in **Figure 9b**). However, the invisible stripes are perceptible after aging due to the blueshift of the longitudinal peak back to the visible region (**Figure 9b**). In the third sample, its initial peak at 860 nm produces a yellow color in the plasmonic film if only the longitudinal peak is excited, primarily induced by the absorption of RF polymer at the short wavelength (left panels in **Figure 9c**). Aging this film leads to interesting yellow to green and blue color changes determined by the longitudinal peak position (**Figure 9c**). The success of the first sample allows us to design and fabricate a thermochromic plasmonic film for displaying encrypted information upon temperature increase (**Figure 9d**).

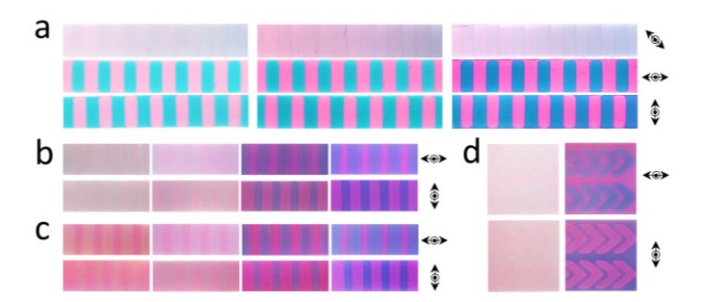


Figure 9. Thermochromic plasmonic films. **(a)** Plasmonic films before (left panels), after selectively etching Fe₃O₄ nanorods (middle panels), and after aging for 36 hours (right panels). The initial peak position of concave Au nanorods is at 645 nm. **(b,c)** Thermochromic plasmonic films made of concave Au nanorods with initial peaks at 760 nm **(b)** and 860 nm **(c)**. The panels from left to right in **(b)** and **(c)** exhibit the thermochromic films before and after etching Fe₃O₄ nanorods and aging for 36 h and 72 h. **(d)** The thermochromic plasmonic films displaying the encrypted images after thermal aging. The black dots and arrows indicate the light propagation direction and polarization, respectively.

4. Conclusions

In summary, we have developed a robust strategy to create pronounced, highly tunable surface concavity on plasmonic nanorods by taking advantage of seed-mediated growth in defined gaps and demonstrated their promising optical properties in designing thermochromic plasmonic films. While the initial negative curvature can be easily controlled by the size of Fe₃O₄ nanorods, the resulting surface concavity can be further tuned by an aging process. Such surface concavity produces a structure-dependent transverse cavity band at a long wavelength with scatteringdominated optical properties. The concave Au nanorods are far from thermodynamic equilibrium but favored by the reduction kinetics, enabling copious thermochromic responses to temperature changes. The creation and reconstruction of concave nanostructures can be readily extended to many metal nanostructures for exquisite structure and surface engineering. Using the concave Au nanorods as responsive building blocks, we have created thermochromic plasmonic films with highly controllable colorimetric responses to temperature changes, which may have interesting applications in anti-counterfeiting, information

encryption, and sensing. The creation and reconstruction of concavity represent a new strategy for designing unconventional nanostructures with advantageous properties desirable for a wide range of applications ranging from smart materials to advanced catalysts.

ASSOCIATED CONTENT

Supporting Information. Experimental details, TEM images, measured extinction spectra, models of structural reconstruction, calculated optical cross-sections of Au nanorods under different orientations and aging states. This material is available free of charge via the internet at http://pubs.acs.org.

AUTHOR INFORMATION

Corresponding Author

* E-mail: yadong.yin@ucr.edu

Author Contributions

The manuscript was written through the contributions of all authors. All authors have given approval to the final version of the manuscript.

Funding Sources

U.S. National Science Foundation (CHE-1808788).

Notes

The authors declare no competing financial interest.

ACKNOWLEDGMENT

The authors are grateful for the financial support from the U.S. National Science Foundation (CHE-1808788).

REFERENCES

- 1. Hentschel, M.; Schäferling, M.; Duan, X.; Giessen, H.; Liu, N., Chiral plasmonics. *Sci. Adv.* **2017**, *3* (5), e1602735.
- 2. Jiang, N.; Zhuo, X.; Wang, J., Active plasmonics: principles, structures, and applications. *Chem. Rev.* **2017**, *118* (6), 3054-3099.
- 3. Kristensen, A.; Yang, J. K.; Bozhevolnyi, S. I.; Link, S.; Nordlander, P.; Halas, N. J.; Mortensen, N. A., Plasmonic colour generation. *Nat. Rev. Mater.* **2016**, *2* (1), 1-14.
- 4. Lee, K.-S.; El-Sayed, M. A., Gold and silver nanoparticles in sensing and imaging: sensitivity of plasmon response to size, shape, and metal composition. *J. Phys. Chem. B* **2006**, *110* (39), 19220-19225.
- 5. Li, Z.; Yin, Y., Stimuli responsive optical nanomaterials. *Adv. Mater.* **2019,** *31* (15), 1807061.
- 6. Stewart, M. E.; Anderton, C. R.; Thompson, L. B.; Maria, J.; Gray, S. K.; Rogers, J. A.; Nuzzo, R. G., Nanostructured plasmonic sensors. *Chem. Rev.* **2008**, *108* (2), 494-521.

- 7. Han, X.; Liu, Y.; Yin, Y., Colorimetric stress memory sensor based on disassembly of gold nanoparticle chains. *Nano Lett.* **2014**, *14* (5), 2466-2470.
- 8. Li, Z.; Yang, F.; Yin, Y., Smart materials by nanoscale magnetic assembly. *Adv. Funct. Mater.* **2020**, *30* (2), 1903467.
- 9. Brongersma, M. L.; Halas, N. J.; Nordlander, P., Plasmon-induced hot carrier science and technology. *Nat. Nanotechnol.* **2015**, *10* (1), 25-34.
- 10. Liu, L.; Gao, Z.; Jiang, B.; Bai, Y.; Wang, W.; Yin, Y., Reversible assembly and dynamic plasmonic tuning of Ag nanoparticles enabled by limited ligand protection. *Nano Lett.* **2018**, *18* (8), 5312-5318.
- 11. Li, Z.; Fan, Q.; Wu, C.; Li, Y.; Cheng, C.; Yin, Y., Magnetically Tunable Plasmon Coupling of Au Nanoshells Enabled by Space-Free Confined Growth. *Nano Lett.* **2020**, *20* (11), 8242-8249.
- 12. Feng, J.; Yang, F.; Wang, X.; Lyu, F.; Li, Z.; Yin, Y., Self aligned anisotropic plasmonic nanostructures. *Adv. Mater.* **2019**, *31* (19), 1900789.
- 13. Liu, L.; Aleisa, R.; Zhang, Y.; Feng, J.; Zheng, Y.; Yin, Y.; Wang, W., Dynamic Color Switching of Plasmonic Nanoparticle Films. *Angew. Chem.* **2019**, *131* (45), 16453-16459.
- 14. Kundu, P. K.; Samanta, D.; Leizrowice, R.; Margulis, B.; Zhao, H.; Börner, M.; Udayabhaskararao, T.; Manna, D.; Klajn, R., Light-controlled self-assembly of non-photoresponsive nanoparticles. *Nat. Chem.* **2015**, 7 (8), 646-652.
- 15. Wang, M.; Gao, C.; He, L.; Lu, Q.; Zhang, J.; Tang, C.; Zorba, S.; Yin, Y., Magnetic tuning of plasmonic excitation of gold nanorods. *J. Am. Chem. Soc.* **2013**, *135* (41), 15302-15305.
- 16. Chow, T. H.; Li, N.; Bai, X.; Zhuo, X.; Shao, L.; Wang, J., Gold nanobipyramids: an emerging and versatile type of plasmonic nanoparticles. *Acc. Chem. Res.* **2019**, *52* (8), 2136-2146.
- 17. Wang, Z.; Yang, G.; Zhang, Z.; Jin, M.; Yin, Y., Selectivity on etching: Creation of highenergy facets on copper nanocrystals for CO2 electrochemical reduction. *ACS nano* **2016**, *10* (4), 4559-4564.

- 18. Berkovitch, N.; Ginzburg, P.; Orenstein, M., Concave plasmonic particles: broad-band geometrical tunability in the near-infrared. *Nano Lett.* **2010**, *10* (4), 1405-1408.
- 19. Haddadnezhad, M.; Yoo, S.; Kim, J.; Kim, J.-M.; Son, J.; Jeong, H. S.; Park, D.; Nam, J.-M.; Park, S., Synthesis and Surface Plasmonic Characterization of Asymmetric Au Split Nanorings. *Nano Lett.* **2020**, *20* (10), 7774-7782.

 20. Yoo, S.; Lee, J.; Kim, J.; Kim, J.-M.; Haddadnezhad, M.; Lee, S.; Choi, S.; Park, D.; Nam, J.-M.; Park, S., Silver Double Nanorings with Circular Hot Zone. *J. Am. Chem. Soc.* **2020**,
- 21. Li, Y.; Lin, H.; Zhou, W.; Sun, L.; Samanta, D.; Mirkin, C. A., Corner-, edge-, and facet-controlled growth of nanocrystals. *Sci. Adv.* **2021,** *7* (3), eabf1410.

142 (28), 12341-12348.

- 22. Velázquez-Salazar, J. J.; Bazán-Díaz, L.; Zhang, Q.; Mendoza-Cruz, R. n.; Montano-Priede, L.; Guisbiers, G.; Large, N.; Link, S.; José-Yacamán, M., Controlled overgrowth of five-fold concave nanoparticles into plasmonic nanostars and their single-particle scattering properties. *ACS nano* **2019**, *13* (9), 10113-10128.
- 23. Jiang, R.; Qin, F.; Liu, Y.; Ling, X. Y.; Guo, J.; Tang, M.; Cheng, S.; Wang, J., Colloidal Gold Nanocups with Orientation Dependent Plasmonic Properties. *Adv. Mater.* **2016**, *28* (30), 6322-6331.
- 24. Wiley, B.; Sun, Y.; Xia, Y., Synthesis of silver nanostructures with controlled shapes and properties. *Acc. Chem. Res.* **2007**, *40* (10), 1067-1076.
- 25. DeSantis, C. J.; Peverly, A. A.; Peters, D. G.; Skrabalak, S. E., Octopods versus concave nanocrystals: control of morphology by manipulating the kinetics of seeded growth via coreduction. *Nano Lett.* **2011**, *11* (5), 2164-2168.
- 26. Zhang, L. F.; Zhong, S. L.; Xu, A. W., Highly branched concave Au/Pd bimetallic nanocrystals with superior electrocatalytic activity and highly efficient SERS enhancement. *Angew. Chem. Int. Ed.* **2013**, *52* (2), 645-649.
- 27. Yu, Y.; Zhang, Q.; Lu, X.; Lee, J. Y., Seed-mediated synthesis of monodisperse concave trisoctahedral gold nanocrystals with controllable sizes. *J. Phys. Chem. C* **2010**, *114* (25), 11119-11126.

- 28. Zhang, Q.; Zhou, Y.; Villarreal, E.; Lin, Y.; Zou, S.; Wang, H., Faceted gold nanorods: nanocuboids, convex nanocuboids, and concave nanocuboids. *Nano Lett.* **2015**, *15* (6), 4161-4169.
 29. Kim, J.; Yoo, S.; Kim, J.-M.; Choi, S.; Kim, J.; Park, S.-J.; Park, D.; Nam, J.-M.; Park, S., Synthesis and Single-Particle Surface-Enhanced Raman Scattering Study of Plasmonic Tripod Nanoframes with Y-Shaped Hot-Zones. *Nano Lett.* **2020**, *20* (6), 4362-4369.
- 30. Yoo, S.; Kim, J.; Choi, S.; Park, D.; Park, S., Two-dimensional nanoframes with dual rims. *Nat. Commun.* **2019**, *10* (5789), 1-8.
- 31. Yin, Y.; Alivisatos, A. P., Colloidal nanocrystal synthesis and the organic–inorganic interface. *Nature* **2005**, *437* (7059), 664-670.
- 32. Li, Z.; Jin, J.; Yang, F.; Song, N.; Yin, Y., Coupling magnetic and plasmonic anisotropy in hybrid nanorods for mechanochromic responses. *Nat. Commun.* **2020**, *11* (2883), 1-11.
- 33. Li, Z.; Ye, Z.; Han, L.; Fan, Q.; Wu, C.; Ding, D.; Xin, H. L.; Myung, N. V.; Yin, Y., Polarization Modulated Multidirectional Photothermal Actuators. *Adv. Mater.* **2021**, *33* (3), 2006367.
- 34. Xu, W.; Wang, M.; Li, Z.; Wang, X.; Wang, Y.; Xing, M.; Yin, Y., Chemical transformation of colloidal nanostructures with morphological preservation by surface-protection with capping ligands. *Nano Lett.* **2017**, *17* (4), 2713-2718.
- 35. Li, T.; Cao, M.; Liang, J.; Xie, X.; Du, G., Mechanism of Base-Catalyzed Resorcinol-Formaldehyde and Phenol-Resorcinol-Formaldehyde Condensation Reactions: A Theoretical Study. *Polymers* **2017**, *9* (9), 426.
- 36. Zhang, G.; Ni, C.; Liu, L.; Zhao, G.; Fina, F.; Irvine, J. T., Macro-mesoporous resorcinol-formaldehyde polymer resins as amorphous metal-free visible light photocatalysts. *J. Mater. Chem. A* **2015**, *3* (30), 15413-15419.
- 37. Gao, C.; Zhang, Q.; Lu, Z.; Yin, Y., Templated synthesis of metal nanorods in silica nanotubes. *J. Am. Chem. Soc.* **2011**, *133* (49), 19706-19709.
- 38. Baghalha, M., The leaching kinetics of an oxide gold ore with iodide/iodine solutions. *Hydrometallurgy* **2012**, *113*, 42-50.

- 39. Qi, P.; Hiskey, J. B., Dissolution kinetics of gold in iodide solutions. *Hydrometallurgy* **1991**, *27* (1), 47-62.
- 40. Chen, L.; Ji, F.; Xu, Y.; He, L.; Mi, Y.; Bao, F.; Sun, B.; Zhang, X.; Zhang, Q., High-yield seedless synthesis of triangular gold nanoplates through oxidative etching. *Nano Lett.* **2014**, *14* (12), 7201-7206.
- 41. Zhang, Q.; Li, N.; Goebl, J.; Lu, Z.; Yin, Y., A systematic study of the synthesis of silver nanoplates: is citrate a "magic" reagent? *J. Am. Chem. Soc.* **2011**, *133* (46), 18931-18939.
- 42. Gilroy, K. D.; Elnabawy, A. O.; Yang, T.-H.; Roling, L. T.; Howe, J.; Mavrikakis, M.; Xia, Y., Thermal stability of metal nanocrystals: An investigation of the surface and bulk reconstructions of Pd concave icosahedra. *Nano Lett.* **2017**, *17* (6), 3655-3661.
- 43. Zhang, J.; Langille, M. R.; Personick, M. L.; Zhang, K.; Li, S.; Mirkin, C. A., Concave cubic gold nanocrystals with high-index facets. *J. Am. Chem. Soc.* **2010**, *132* (40), 14012-14014.
- 44. Bin, D.-S.; Chi, Z.-X.; Li, Y.; Zhang, K.; Yang, X.; Sun, Y.-G.; Piao, J.-Y.; Cao, A.-M.; Wan, L.-J., Controlling the compositional chemistry in single nanoparticles for functional hollow carbon nanospheres. *J. Am. Chem. Soc.* **2017**, *139* (38), 13492-13498.
- 45. Métraux, G. S.; Mirkin, C. A., Rapid thermal synthesis of silver nanoprisms with chemically tailorable thickness. *Adv. Mater.* **2005**, *17* (4), 412-415.
- 46. Jin, R.; Cao, Y. C.; Hao, E.; Métraux, G. S.; Schatz, G. C.; Mirkin, C. A., Controlling anisotropic nanoparticle growth through plasmon excitation. *Nature* **2003**, *425* (6957), 487-490.
- 47. Zhang, Q.; Ge, J.; Pham, T.; Goebl, J.; Hu, Y.; Lu, Z.; Yin, Y., Reconstruction of silver nanoplates by UV irradiation: tailored optical properties and enhanced stability. *Angew. Chem. Int. Ed.* **2009**, *48* (19), 3516-3519.
- 48. An, J.; Tang, B.; Zheng, X.; Zhou, J.; Dong, F.; Xu, S.; Wang, Y.; Zhao, B.; Xu, W., Sculpturing effect of chloride ions in shape transformation from triangular to discal silver nanoplates. *J. Phys. Chem. C* **2008**, *112* (39), 15176-15182.
- 49. Zhang, X.; Li, Z.; Feng, J.; Yang, F.; Wu, C.; Fan, Q.; Zhou, S.; Yin, Y., Dynamic Tuning of Optical Transmittance of 1D Colloidal

Assemblies of Magnetic Nanostructures. *Adv. Intell. Syst.* **2019**, *1* (8), 1900099.

50. Wang, M.; Yin, Y., Magnetically responsive nanostructures with tunable optical properties. *J. Am. Chem. Soc.* **2016**, *138* (20), 6315-6323.

Table of Contents

